Materials Advances

ROYAL SOCIETY OF CHEMISTRY

PAPER

View Article Online
View Journal | View Issue

Cite this: *Mater. Adv.*, 2024, 5, 6170

Electrochemical performance enhancement of MnO_2 nanowires through silver incorporation for next-generation supercapacitors

Muhammad Usman Khalid,[a] Sonia Zulfiqar,[bc] M. Naziruddin Khan,[d] Imran Shakir,[d] Muhammad Farooq Warsi *[a] and Eric W. Cochran *[c]

Increased demand for effective energy storage systems emphasizes the urgency to overcome the bottlenecks of existing technology. Supercapacitors (SCs), owing to their high specific power and fast charging/discharging capabilities, are perfect candidates for future energy applications but their low energy density makes them impractical for commercial applications. Because of their high energy density and variable oxidation states, transition metal oxides (TMOs) have great potential as supercapacitor electrode materials. But for practical applications, their poor intrinsic conductivity needs to be improved. Noble metal doping offers a compelling method to raise the conductivity and structural stability of TMOs. Herein, we have prepared Ag_xMnO_2 (x = 0.05, 0.10, and 0.15) to improve the conductivity and structural stability of the electro-active material. FESEM micrographs exhibit cracks on the nanowire (NW) surface by Ag doping, proposing less dead volume. Ag doping also fortified electrode pulverization during charging/discharging cycles by imparting structural stability. These properties enabled $Ag_{0.05}MnO_2$ NWs to demonstrate a specific capacitance of 1027 F g^{-1} at a current density of 1 A g^{-1}. The electrode also retained a capacitance of 93.16% after 10 000 GCD cycles@12 A g^{-1} along with 86% rate capability at 9 A g^{-1}. By tackling critical difficulties such as poor conductivity and structural stability, this study advances energy storage technologies and lays the groundwork for the creation of high-performance supercapacitors for future energy applications.

Received 5th February 2024,
Accepted 7th June 2024

DOI: 10.1039/d4ma00118d

rsc.li/materials-advances

1. Introduction

Addressing the escalating environmental pollution concerns resulting from increased fossil fuel consumption highlights the growing importance of renewable energy storage devices to fulfill next-generation energy demands.[1–4] Fossil fuel burning produces almost 35 billion tons of CO_2 per annum, which is adversely affecting the air quality index.[5,6] The combustion of fossil fuels is also damaging soil and water sources. Materials scientists and researchers are trying to develop green and sustainable energy production systems such as hydro-power, solar cells, and windmills.[7,8] However, these energy sources are climate dependent. Therefore, it is challenging to construct energy storage systems to meet the ever-increasing energy demands. Modern devices, such as portable electronics, medical equipment, smartphones, load-managing systems, and hybrid vehicles, necessitate immediate access to high power. This requirement presents a barrier that rechargeable batteries cannot adequately meet.

Supercapacitors are excellent rechargeable energy storage systems that can power up modern electronics and electrical gadgets.[9,10] They have superior power density than rechargeable batteries.[11] Supercapacitors have received a lot of interest for their potential as replacements to conventional capacitors and rechargeable batteries. They have remarkable characteristics such as high specific power, extended cycle life, outstanding rate capability, and quick charging/discharging capabilities. These distinct properties make supercapacitors ideal candidates for applications in new energy systems such as wearable electronic gadgets, load management systems, and powering off-grid homes. Furthermore, supercapacitors provide energy to power up electric vehicles through increased specific power. However, supercapacitors have low energy density as compared to rechargeable batteries. The energy density is related to the specific capacitance and potential window of a supercapacitor

[a] *Institute of Chemistry, Baghdad-ul-Jadeed Campus, The Islamia University of Bahawalpur, Bahawalpur 63100, Pakistan. E-mail: farooq.warsi@iub.edu.pk*
[b] *Department of Chemistry, Faculty of Science, University of Ostrava, 30. Dubna 22, Ostrava 701 03, Czech Republic*
[c] *Department of Chemical and Biological Engineering, Iowa State University, Sweeney Hall, 618 Bissell Road, Ames, Iowa 50011, USA. E-mail: ecochran@iastate.edu*
[d] *Department of Physics, Faculty of Science, Islamic University of Madinah, Madinah, 42351, Saudi Arabia*

by the equation $E = \frac{1}{2}CV^2$. So, the energy density could be improved either by increasing specific capacitance or by extending the voltage window. Recent research in the domain of supercapacitors has witnessed substantial advances in the use of transition metal oxides and sulfides as electrode materials. Studies by Vilhal *et al.*, Prabhu *et al.*, Jiang *et al.*, Sun *et al.*, Pappu *et al.*, and Van *et al.* have shown that NiO, CuO, and Cu doped ceria, manganese oxide/carbon composite cobalt manganese oxide, and Ni–Co binary sulfides have potential electrochemical characteristics for improving energy storage performance in supercapacitors.[12–17] Furthermore, comprehensive studies by Melkiyur *et al.* and Imran *et al.* have summarized the existing state-of-the-art and future prospects of transition metal oxides/sulfides and manganese oxide/sulfide in supercapacitor technology respectively.[18,19]

Especially, transition metal oxides have gained substantial interest as supercapacitor electrode materials because of their faradaic redox nature to store charge, which improves the energy density of the supercapacitor. Sana *et al.* demonstrated that Ag–V_2O_5 exhibited a specific capacitance of 516.6 F g^{-1}@ 1 A g^{-1} current density.[20] Wang *et al.* reported that Co_3O_4 nanowires demonstrated a specific capacitance of 880.2 F g^{-1}@ 1 A g^{-1} current density with a rate capability of 70%@ 20 A g^{-1}.[21] Liu *et al.* reported that the Ag–MnO_2/rGO composite exhibited a specific capacitance of 804.6@1 A g^{-1}.[22] Ozoemena *et al.* demonstrated that K^+/Na^+ pre-intercalated MnO_2 NWs exhibited a specific capacitance of 124 F g^{-1} in KOH electrolyte.[23] Among TMOs, manganese dioxide (MnO_2) nanostructures have attracted great attraction as electrode materials for supercapacitors, thanks to their economic and environmentally friendly nature, theoretical capacitance (1370 F g^{-1}), and non-toxicity. MnO_2 nanostructures exist in a variety of crystallographic forms (α, β, γ, and δ).[24] These crystallographic forms are distinct from each other by the linkage of basic [MnO_6] octahedra. In α, β, and γ MnO_2, [MnO_6] octahedron links in such a way that it forms (2 × 2 and 1 × 1), (1 × 1), and (2 × 1) tunnels respectively. α-MnO_2 is regarded as a potential candidate for supercapacitor applications due to a larger tunnel structure of 4.62 Å.[25] The larger tunnel structure makes electrolyte ion insertion and de-insertion quite easy resulting in fast charging/discharging rates. However, the α-phase of MnO_2 suffers from stability issues and transforms into other phases of MnO_2.[26,27] Previous studies have shown that the α phase of MnO_2 is stabilized by doping with larger ions.[28–30] MnO_2 also has poor electronic conductivity like other transition metal oxides.[31] Ag doping in MnO_2 has been proved to be beneficial due to excellent conductivity of silver which contributes to the overall conductivity enhancement of the electrode material. Ag^+ ions have larger ionic radii (1.15 Å) due to which they are able to stabilize α-MnO_2. Additionally, hybridization between Ag 4d and O 2p induces new states between conduction and valence bands. The p–d repulsion is so high that it moves the Fermi level towards the conduction band resulting in an ease in electron transfer to the conduction band. Oxygen and interstitial defects produced by silver doping also induce new occupied states between conduction and valence band resulting in an upward movement of the Fermi level. Silver doping also induced n-type characteristics in p-type MnO_2.[32] Consequently, silver is expected to induce structural stability to maintain the lifespan of SCs over longer charging/discharging cycles along with improvement in conductivity. Structural stability could also be obtained by doping alkali metal ions but Ag 4d and O 2p hybridization which contributes towards conductivity improvement makes Ag preferable over alkali metal ions and transition metal ions. Moreover, silver is the most conductive metal in the periodic table.[33] Additionally, silver being a redox active material could introduce more redox active sites in the electrode material contributing to improved pseudocapacitance, leading to enhanced energy density. Owing to these characteristics, silver is considered as an excellent dopant for MnO_2. The synergistic effect of silver's excellent conductivity and α-MnO_2's pseudocapacitance and large tunnel structure could improve energy density along with power density, enabling supercapacitors applicable where quick and longer energy discharge is needed. Rahman *et al.* prepared silver doped MnO_2@carbon cloth for supercapacitor applications. The electrode demonstrated a capacitance of 350 F g^{-1}@1 A g^{-1} current density. They also reported the performance of a Ag–MnO_2/activated carbon asymmetric supercapacitor device. The device demonstrated an energy density of 54 W h kg^{-1} in a 0–2 V potential window.[34] Zhang *et al.* assessed the supercapacitor performance of silver nanoparticle loaded MnO_2 nanosheets. Ag–MnO_2 exhibited a capacitance of 272 F g^{-1}@10 mV s^{-1}, which is three times higher than that of the undoped MnO_2 (90 F g^{-1}) in 1 M Na_2SO_4 electrolyte.[35] Dai *et al.* prepared silver nanoparticles embedded in MnO_2 nanowires and studied their electrochemical supercapacitor properties. The electrode material demonstrated a specific capacitance of 1230 F g^{-1}@1 mV s^{-1} scan rate along with a capacitance retention of almost 91% after 10 K charging/discharging cycles.[36]

In this research, we have studied the consequences of varying the amount of silver on the structural and supercapacitor performance of MnO_2. Ag doping in MnO_2 is believed to demonstrate better structural stability and electrochemical performance. Ag doping has tuned the structure of MnO_2 which is confirmed through characterization techniques like XRD, XPS, and FTIR. FESEM micrographs have shown that the NW surface becomes rough after Ag doping, which is expected to provide more redox active sites for electrolyte ions. Ag doping in MnO_2 NWs showed an increase in surface area as confirmed by BET analysis. It was observed that the electrochemical performance of MnO_2 NWs showed an improvement with an optimum silver concentration of 0.05, therefore, MnO_2 doping with an optimum dopant concentration can improve electrochemical performance.

2. Experimental

2.1. Materials

Potassium permanganate ($KMnO_4$, Daejung, 98%), ammonium persulfate [$(NH_4)_2S_2O_8$, Merck, 98%], nitric acid (HNO_3, Merck,

70%), silver nitrate ($AgNO_3$, Merck, 98%), absolute ethanol (C_2H_5OH, Merck, 98%) and deionized (DI) water.

2.2. Synthesis of Ag_xMnO_2 nanowires

MnO_2 NWs were synthesized through a low temperature hydrothermal treatment. A uniform aqueous solution of $KMnO_4$ was prepared by dissolving it (4 g) in DI water with continuous stirring. Subsequently, aqueous solution of ammonium persulfate was prepared by dissolving it (2 g) in a separate beaker. This solution was slowly added to the aqueous solution of $KMnO_4$. After that, 1 cm^3 of nitric acid was added to the above mixture. The total volume of the mixture was made up to 80 cm^3 by the addition of some more DI water. The resulting mixture was then transferred to a Teflon-lined autoclave for heat treatment at 180 °C for 16 h. Afterwards, the mixture was washed multiple times with DI water and ethanol to eliminate impurities and neutralize the solution. Finally, the precipitates were dried overnight at 100 °C. The resulting nanowires were finely ground into powder and stored for further characterization and potential application. To introduce Ag into MnO_2, the same protocol was employed with different Mn : Ag molar ratios (1 : 0.05, 1 : 0.1, 1 : 0.15). Ag_xMnO_2 NWs grow *via* Ostwald ripening.[37,38] A schematic illustration for the formation mechanism of Ag_xMnO_2 NWs is depicted in Fig. 1.

2.3. Electrode preparation

Sonication was used to prepare binder-free electrodes of MnO_2 NWs and Ag_xMnO_2 NWs on the nickel foam. In a typical synthesis procedure, MnO_2 NW paste in DI water was created by sonication for 60 min. The homogenized paste was then transferred on HCl treated and washed nickel foam using a micropipette. The electroactive material-loaded nickel foam was then placed in an oven at 50 °C for complete removal of DI water. Subsequent evaluation of electrochemical supercapacitor performance was done using the prepared electrode.

2.4. Electrochemical studies

Electrochemical performance of MnO_2 NWs and Ag_xMnO_2 NWs was tested in a half-cell configuration using 1 M Na_2SO_4. Cyclic voltammetric (CV) response was assessed in a potential range 0–0.6 V. GCD measurements were performed in order to assess the charging/discharging behavior of the electrodes. Additionally, the effect of various current densities on $Ag_{0.05}MnO_2$ was also studied. Measurements using electrochemical impedance spectroscopy (EIS) were conducted between 0.1 Hz and 100 kHz frequency.

2.5. Characterization

Structural investigations of Ag_xMnO_2 NWs were conducted on a LabX XRD-6100 X-ray diffractometer. Functional group identification was performed using an IR Affnity-1S spectrophotometer. Studies on morphology were executed using a ZEISS LEO SUPRA 55 field emission scanning electron microscope. Elemental presence was evaluated using a JEOL JCM-6000Plus SEM. Transmission electron microscopy (TEM) was performed using a JEOL JSM 2100 transmission electron microscope operating at 200 kV. The XPS measurements were carried out using a Kratos Amicus/ESCA 3400 instrument. A DuPont type analyzer was used to examine the energy of photoelectrons that were emitted at 0° from the surface normal after the sample was exposed to 240 W unmonochromated Mg Kα X-rays at a pass energy of 150 eV. Using the Micromeritics ASAP 2020 Physisorption analyzer, the BET surface area of the samples was determined. Electrochemical performance of the as synthesized electrodes was tested on GAMRY interface 5000E.

3. Results and discussion

3.1. X-ray diffraction (XRD)

Structural investigations and crystallite size determination of bare and doped MnO_2 NWs have been carried out by XRD analysis.[39] The XRD spectra of Ag_xMnO_2 NWs are shown in Fig. 2(a). All the diffraction peaks are generated by (220), (310), (400), (211), (330), (420), (301), (510), (411), (600), (521), (002), (541), and (312) diffraction planes of tetragonal MnO_2 according to ICDD card # 00-044-0141.[40] The intense diffraction peaks indicated good crystallinity and the intensity was observed to decrease through Ag doping. This decrease in intensity showed that the crystallinity is disturbed by doping. This could be attributed to the insertion of Ag^+ ions into the MnO_2 lattice.[41] This intensity reduction may be associated with the fact that doping can induce defects and dislocations in the crystal lattice. Defects, such as vacancies or interstitials, introduce local atomic rearrangements, while dislocations are line defects caused by lattice mismatch. Both defects and dislocations scatter X-rays, leading to a decrease in peak intensity. Moreover,

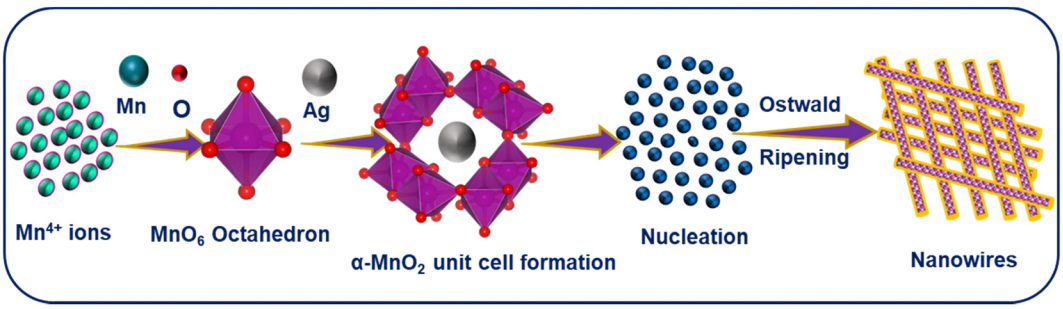

Fig. 1 A schematic illustration for the formation mechanism of Ag_xMnO_2 NWs.

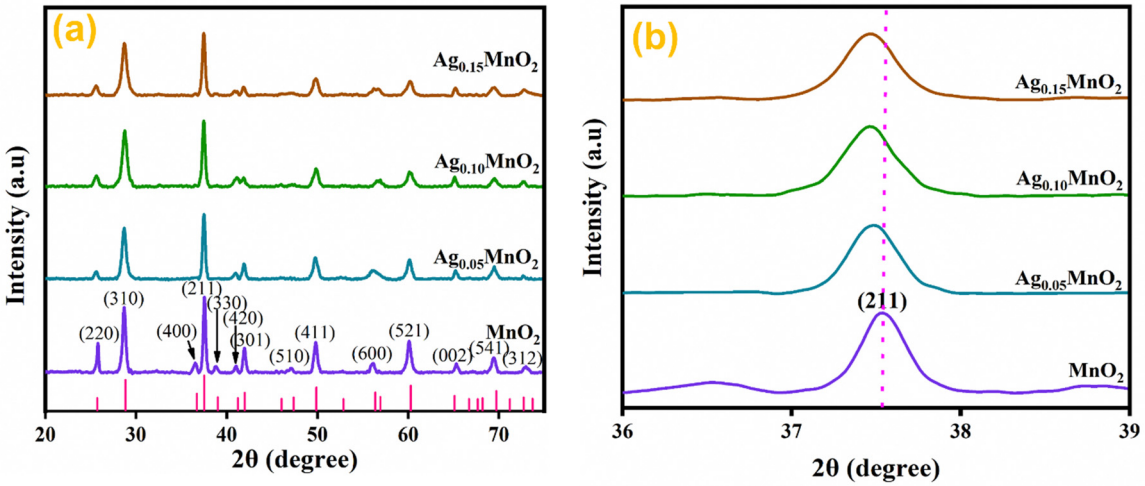

Fig. 2 (a) XRD patterns of bare and Ag doped MnO_2 NWs, (b) enlarged view of diffraction peak from (211) diffraction plane.

doping can lead to the formation of amorphous or poorly crystalline regions within the material. Fig. 2(b) shows the magnified view of the diffraction peak associated with the (211) plane. With silver doping, the diffraction peak was shifted towards a lower angle. This shifting is attributed to ionic radii difference between Ag^{+} (1.15 Å) and Mn^{4+} (0.53 Å).[42] When Ag atoms substitute Mn atoms in the MnO_2 lattice, the average atomic size increases. This increase in atomic size can cause lattice expansion, leading to a shift in the XRD peaks towards lower diffraction angles.[43–45] The average crystallite size "*D*" was calculated using the Debye Scherrer equation.[46,47]

$$D = K\lambda/\beta\cos\theta \quad (1)$$

The calculated crystallite sizes for Ag_xMnO_2 NWs (x = 0, 0.05, 0.10, and 0.15) were found to be 13.65 nm, 13.20 nm, 12.80 nm, and 12.50 nm, respectively. Upon increasing the Ag concentration, the crystallite size decreased, and is well consistent with the previous literature.[48] The surface area of all the samples was calculated from XRD data using the eqn (2).[49,50]

$$S = 6000/(D \times \rho_x) \quad (2)$$

The calculated surface area of MnO_2, $Ag_{0.05}MnO_2$, $Ag_{0.10}MnO_2$, and $Ag_{0.15}MnO_2$ NWs was found to be 57.2 $m^2\ g^{-1}$, 73.1 $m^2\ g^{-1}$, 68.3 $m^2\ g^{-1}$, and 63.7 $m^2\ g^{-1}$, respectively.

3.2. Fourier transform infrared (FTIR) spectroscopy

Functional groups of pristine, and Ag_xMnO_2 NWs were confirmed by FTIR technique.[51] FTIR spectra of Ag_xMnO_2 NWs are given in Fig. 3. All the absorption bands are in good agreement with the literature.[28] The absorption bands below 1000 cm^{-1} (low frequency region) confirmed the successful synthesis of MnO_6 octahedra.[52] Briefly, the absorption bands located at 465 cm^{-1} and 512 cm^{-1} are ascribed to Mn–O stretching vibration. The absorption band located at 702 cm^{-1} is attributed to the stretching vibration of Mn–O–Mn, suggesting the formation of MnO_6 octahedra. These absorption bands were located at slightly different positions for the Ag doped samples.

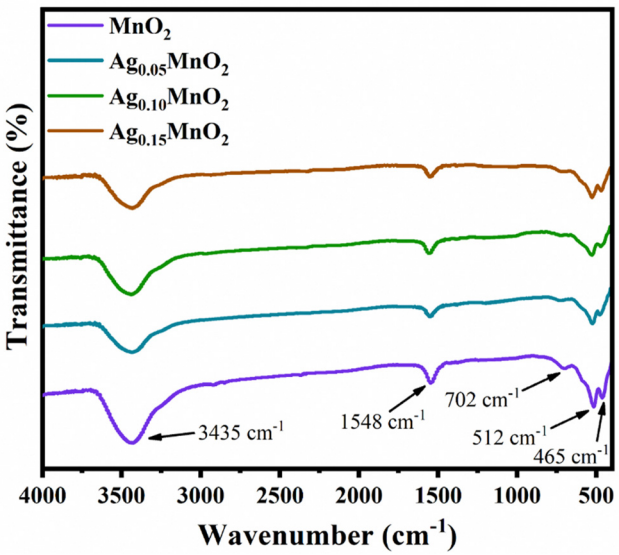

Fig. 3 FTIR spectra of Ag_xMnO_2 NWs.

This illustrates that Ag has been successfully doped into MnO_2. The band at 1548 cm^{-1} is due to Mn–O–H vibration.[53] The intensity decrease with doping indicated that oxygen vacancies are produced. In addition, the band positioned at 3435 cm^{-1} is due to the stretching vibration of the O–H bond.

3.3. Field emission scanning electron microscopy (FESEM)

Morphology of Ag_xMnO_2 NWs was evaluated by FESEM analysis.[54] The FESEM micrograph of pristine MnO_2 showed the nanowires morphology as depicted in Fig. 4(a). Pristine nanowires are ultrathin as well as ultralong having a diameter below 50 nm. Fig. 4(b)–(d) are the FESEM micrographs for MnO_2 NWs doped with different concentrations of silver. Silver doping has made the surface rough, and aggregation has also taken place. The aggregation is resulted from high surface charge.[55,56] The augmented surface charge could be attributed

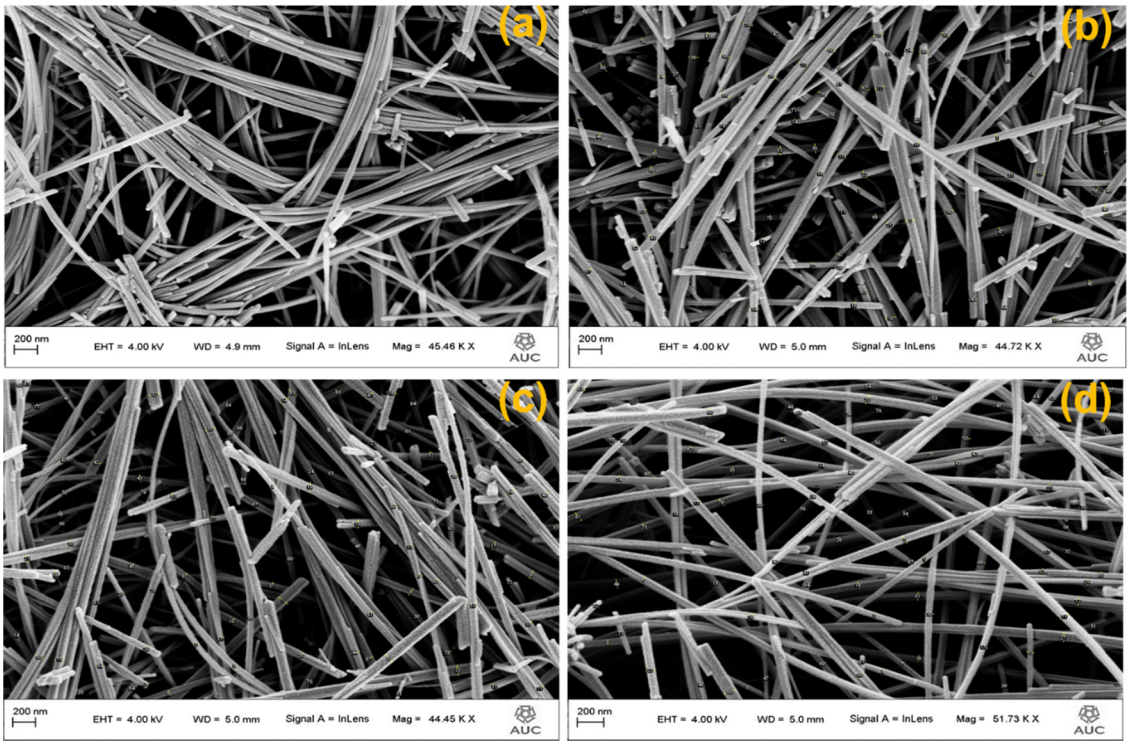

Fig. 4 FESEM images of (a) MnO_2, (b) $Ag_{0.05}MnO_2$, (c) $Ag_{0.10}MnO_2$, (d) $Ag_{0.15}MnO_2$.

to greater ion concentration and reduced pH, as $AgNO_3$ aqueous solution is acidic. It is generally understood that a change in pH value has a significant impact on surface charge (negative or positive). Augmented ionic strength will decrease or remove the repulsive energy barrier, resulting in fast aggregation.[57] Diameters of pristine nanowires are below 50 nm. For Ag doped MnO_2 nanowires, the diameter ranges between 50 and 70 nm.

3.4. High resolution transmission electron microscopy (HRTEM)

HRTEM analysis was performed to study the in-depth morphology and diameter of nanowires.[58] HRTEM images of MnO_2 and $Ag_{0.05}MnO_2$ are illustrated in Fig. 5(a) and (b). MnO_2 and $Ag_{0.05}MnO_2$ nanowires average diameter measured using ImageJ software was found to be 31 nm and 38 nm respectively. TEM images of MnO_2 and $Ag_{0.05}MnO_2$ demonstrate that both the samples have grown nanowires. The slight increase in diameter for $Ag_{0.05}MnO_2$ is credited to the stronger diffusion of Ag^+ ions in the MnO_2 structure.[59] This diffusion is also confirmed by the non-existence of silver particles on the nanowire surface. Fig. 5(c) and (d) demonstrate the selected area diffraction (SAD) pattern of MnO_2 and $Ag_{0.05}MnO_2$. It is clear that both the samples are crystalline and are consistent with the XRD diffractogram. Fig. 5(c) and (d) (inset) illustrate the lattice fringes showing the interplanar spacing (d). MnO_2 has well resolved lattice fringes with the interplanar distance (d = 0.245 nm). While the inter-planar distance for $Ag_{0.05}MnO_2$ is 0.249 nm. This increase is credited to the stress and lattice expansion caused by the diffusion of Ag^+ ions in MnO_2 crystal as confirmed by XRD peak shifting towards lower angle.[60,61] The lattice fringes of $Ag_{0.05}MnO_2$ (Fig. 5(d)) shows that crystallinity of MnO_2 NWs has reduced with Ag doping, which is also confirmed by XRD diffractogram.

3.5. Energy dispersive X-ray (EDX) spectroscopy

Elemental detection of Ag_xMnO_2 NWs was done by EDX technique[62] and the results are presented in Fig. 6. The EDX analysis of MnO_2 NWs revealed de-excitation peaks corresponding to the manganese and oxygen atoms. This confirms that the pristine MnO_2 sample is free from any impurities since the detected peaks exclusively correspond to the elemental composition of Mn and O. However, an unlabeled peak is observed in the spectrum positioned between 3–4 keV. It is attributed to the de-excitation of potassium atoms. The potassium peak originated from the precursor salt used in the synthesis of the MnO_2 NWs. These atoms are believed to reside within the tunnel structure of the nanowires, indicating that they are incorporated into the material during the synthesis process to stabilize the α-phase of MnO_2. The EDX analysis of Ag-doped MnO_2 NWs samples presented in Fig. 6(b)–(d) show the presence of both manganese and oxygen, similar to the pristine sample. However, in addition to peaks associated with manganese and oxygen, de-excitation peaks corresponding to silver atoms are also observed. These peaks indicate the successful incorporation of silver as a dopant into the MnO_2 matrix during the synthesis process. The presence of varied intensity de-excitation peaks for Ag in the EDX spectra was observed by varying the dopant concentration. This confirms that the

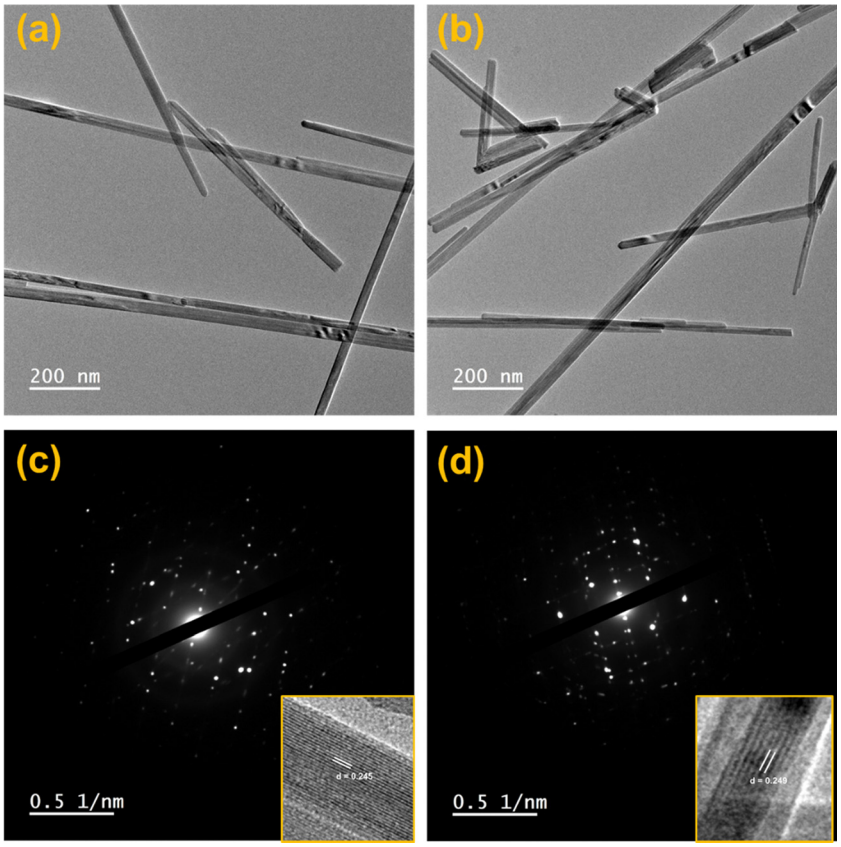

Fig. 5 (a) HRTEM image of MnO_2, (b) HRTEM image of $Ag_{0.05}MnO_2$, (c) SAD pattern of MnO_2, (d) SAD pattern of $Ag_{0.05}MnO_2$.

amount of silver incorporated in the MnO_2 matrix can be varied and controlled by adjusting the dopant concentration during the synthesis process.

3.6. X-ray photoelectron spectroscopy (XPS)

The elemental composition of $Ag_{0.05}MnO_2$ NWs was further confirmed by XPS studies.[63] XPS spectra of the sample are depicted in Fig. 7. Fig. 7(a) shows the XPS spectrum of Mn 2p in $Ag_{0.05}MnO_2$. There has been observed a peak at 642.2 eV that is associated with Mn $2p_{3/2}$. The other peak located at 653.9 eV is associated with Mn $2p_{1/2}$. Spin energy separation of almost 11.7 eV between spin–orbit doublet suggests that Mn exists in +4 oxidation state.[64–66] Fig. 7(b) and (c) show the XPS spectra of O 1s and K 2p in $Ag_{0.05}$ MnO_2. The XPS spectrum of O 1s showed a peak at 529.9 eV along with a shoulder peak around 530.7 eV. The peak at 529.9 eV is ascribed to the structural oxygen while the peak around 530.68 eV is associated with the oxygen of the hydroxyl group.[67] Fig. 7(c) reveals that K atoms from precursor $KMnO_4$ residing in α-MnO_2 tunnels were also detected by the XPS spectrum of K 2p.[68] Fig. 7(d) displays the XPS spectrum of Ag 3d. There has been observed a peak located at 367.5 eV and is associated with Ag $3d_{5/2}$, which clearly suggests that Ag exists as an Ag^+ ion.[69] The other peak located at 373.7 eV is ascribed to Ag $3d_{3/2}$.[70] This shows that Ag has been successfully doped in MnO_2 NWs. The theoretical doping concentration of Ag for $Ag_{0.05}MnO_2$ was 9.58 wt%, while the actual doping concentration calculated by XPS and EDX spectra was found to be 8.71 wt%.

3.7. Current–voltage (*I*–*V*) studies

By applying voltage (*V*) we observed the current (*I*) response of bare and doped MnO_2 NWs. *I*–*V* profiles are depicted in Fig. 8. Conductivity of bare and doped MnO_2 NWs has been calculated using eqn (3).

$$\sigma = \frac{L}{RA} \tag{3}$$

It is also clear from *I*–*V* profile that with Ag doping, the *I*–*V* curve becomes more vertical suggesting an increased current under applied voltage. Conductivity values of bare and doped samples are shown in Table 1. An increase in the conductivity of MnO_2 is observed with Ag doping. This increase is ascribed to defects (oxygen vacancies) which are generated to balance the charge. Generation of oxygen vacancies left behind electrons. Consequently, charge carrier concentration increases which is confirmed by Mott–Schottky analysis, giving rise to an increase in the conductivity of MnO_2 NWs. However, at higher doping concentrations, a large number of defects are generated which leads to increased charge scattering. Thus, giving rise to a decrease in conductivity.[71]

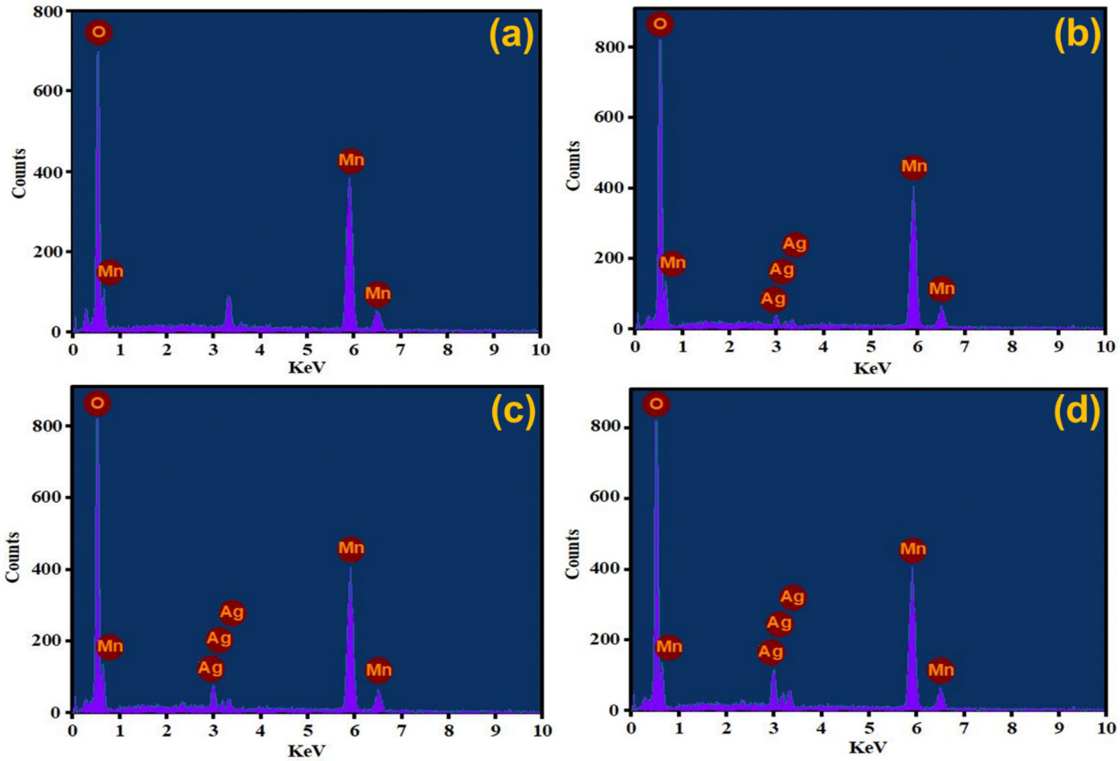

Fig. 6 EDX spectra of (a) MnO_2, (b) $Ag_{0.05}MnO_2$, (c) $Ag_{0.10}MnO_2$, (d) $Ag_{0.15}MnO_2$.

3.8. Physisorption analysis

The effect of doping and composite formation on the specific surface area was investigated through BET analysis.[72] BET measurements were carried out with nitrogen at 77 K. BET isotherms of pristine MnO_2 NWs, and $Ag_{0.05}MnO_2$ NWs are shown in Fig. 9. Pristine and doped samples exhibited the isotherms that resemble the type III isotherm of IUPAC having a H3 hysteresis loop. Rapid higher adsorption at higher relative pressure indicates the presence of small pores in the samples. Both the samples displayed the same type of adsorption/desorption trend, however, the amount of gas adsorbed in Ag doped MnO_2 sample is higher than the pristine MnO_2 NWs. This showed that doping MnO_2 with noble metal is a good way to improve the surface area. The BET surface area of $Ag_{0.05}MnO_2$ NWs is 74 $m^2\ g^{-1}$, which is superior to the surface area of pristine MnO_2 NWs. During the synthesis process, the introduction of noble metal (Ag) can influence the growth and arrangement of the material's microstructure, resulting in the formation of pores or voids. These pores contribute to the increased surface area as they provide additional sites for reactant molecules to interact with the material.

3.9. Electrochemical measurements

Electrochemical measurements of Ag_xMnO_2 NWs were executed to assess the supercapacitor performance of the as-prepared samples. For electrochemical measurements the electro-active material was deposited on 3-D nickel foam (NF). Cyclic voltammetry (CV), galvanostatic charge/discharge (GCD), and electrochemical impedance spectroscopy (EIS) were performed to evaluate the supercapacitor performance of the electrodes. CV measurements for Ag_xMnO_2 (x = 0, 0.05, 0.10, 0.15) were performed to get a better understanding of the electron transfer rate, and redox reactions involved at electrode–electrolyte interface. CV is also used to get an estimation of the appropriate potential window. CV measurements were performed in a potential window 0–0.6 V in 1 M Na_2SO_4 using platinum as the counter electrode, and Ag/AgCl as the reference electrode in a half-cell configuration.

CV profiles of Ag_xMnO_2 are shown in Fig. 10. An anodic peak is observed in the positive current region while the cathodic peak is observed in the negative current region. The bumps in CV curves confirmed the reversible faradaic reaction. The possible electrode reaction may be explained by two different pathways.

The first pathway is the adsorption/desorption of electrolyte ions (Na^+) at the electrode–electrolyte interface and is represented below.

$$MnO_2\ \text{surface} + Na^+ + e^- \rightarrow (MnO_2{}^-Na^+)\ \text{surface}$$

The second pathway involves the insertion/disinsertion of electrolyte ions (Na^+) and protons (H^+) in the bulk involving a redox reaction and is represented below.

$$MnO_2\ \text{bulk} + Na^+ + e^- \rightarrow (MnOONa)\ \text{bulk}$$

Comparative CV measurements for Ag_xMnO_2 NWs were performed at 50 mV s^{-1} scan rate and are displayed in

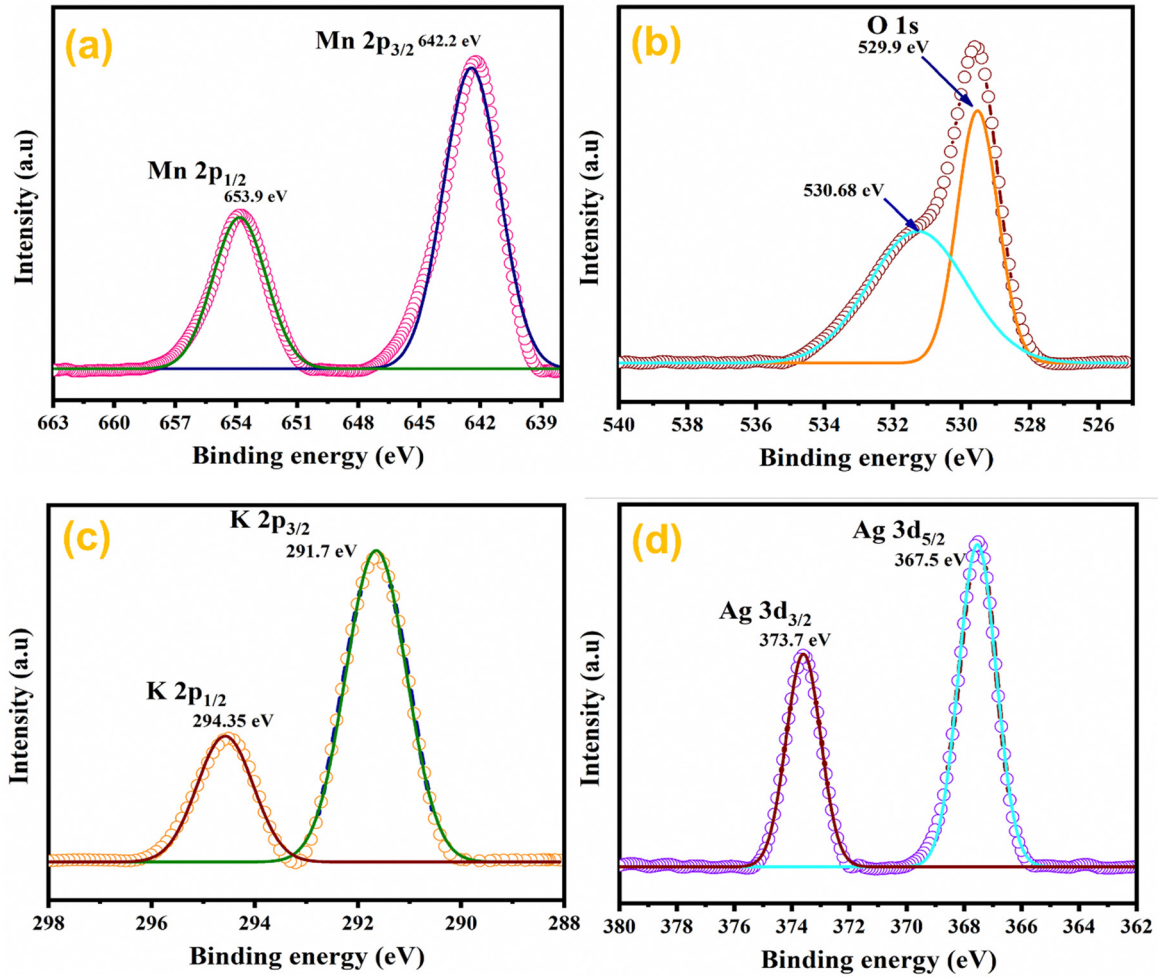

Fig. 7 XPS spectra of $Ag_{0.05}MnO_2$ nanowires.

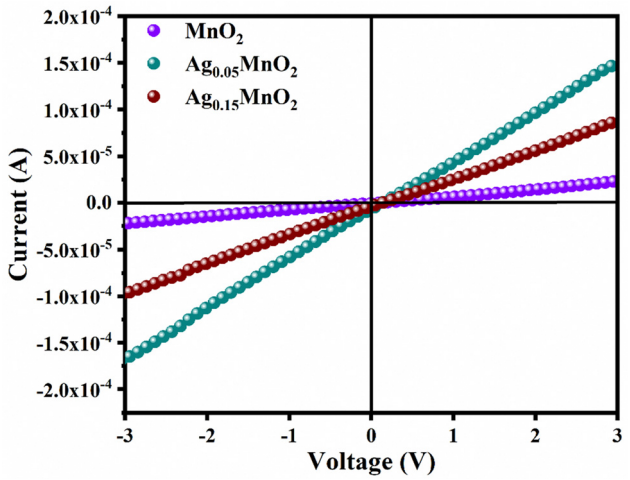

Fig. 8 *I–V* profiles of bare and doped MnO_2 NWs.

Table 1 Electrical conductivity and charge carrier density of Ag_xMnO_2 NWs

S. no.	Sample name	Electrical conductivity (S cm^{-1})	Charge carrier density (cm^{-3})
1	MnO_2	2.90×10^{-5}	1.48×10^{26}
2	$Ag_{0.05}MnO_2$	1.5×10^{-3}	1.20×10^{27}
3	$Ag_{0.15}MnO_2$	5.2×10^{-4}	2.01×10^{28}

Fig. 10(a). The $Ag_{0.05}MnO_2$ electrode showed the greatest integral area among all the samples. The amplified area under the curve is credited to the improved conductivity, thanks to the silver. The presence of silver imparts a new channel for rapid electron transfer by lowering the intrinsic resistivity. In addition, the amplified loop area may be credited to the increased surface area, which will offer more active sites for electrolyte ions to be adsorbed. It is evident from Fig. 10(a) that as the silver concentration increases beyond 0.05 molar, the current response of the electro-active material decreases at 50 mV s^{-1} scan rate and is well consistent with the previous literature.[1] Excessive doping can result in a higher concentration of charge carriers. These carriers can screen the electric field, reducing the effective electric field experienced by the remaining charges and, consequently, the amount of charge that can be stored.

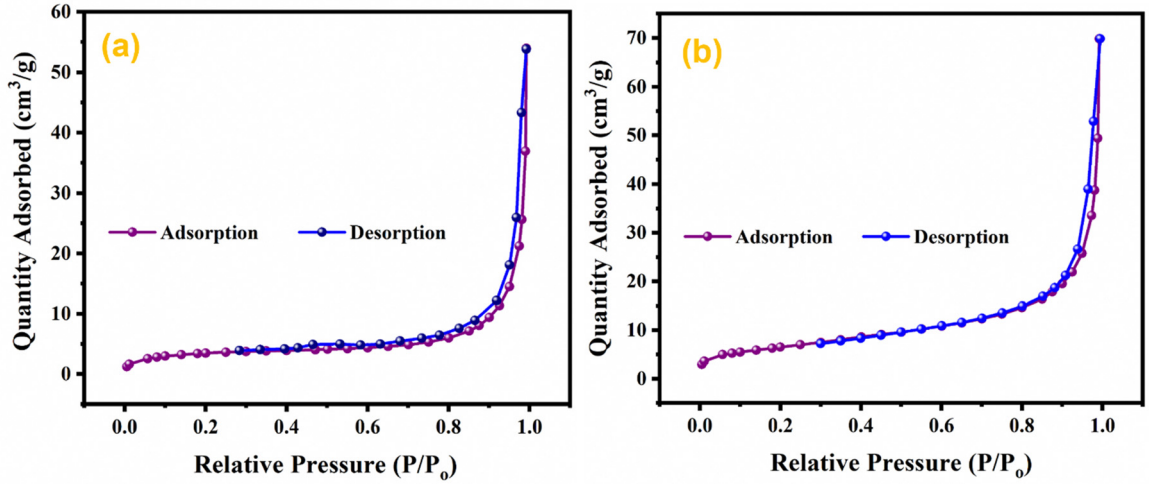

Fig. 9 BET isotherms of (a) MnO_2, (b) $Ag_{0.05}MnO_2$.

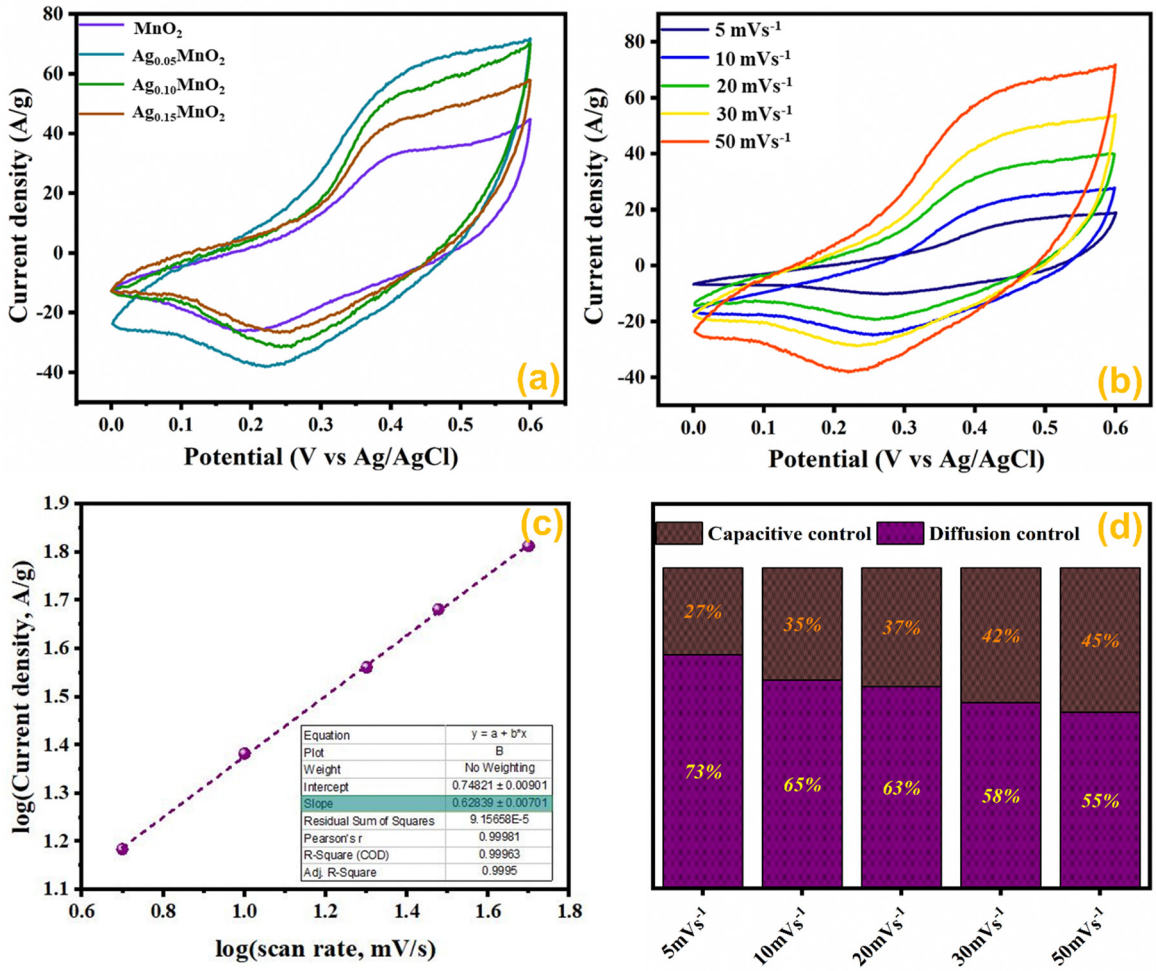

Fig. 10 (a) CV profile of Ag_xMnO_2 NWs, (b) CV profile of $Ag_{0.05}MnO_2$ at various scan rates, (c) log *i* *vs.* log ν graph of $Ag_{0.05}MnO_2$, and (d) impact of the scan rate on the prominent charge storage process of $Ag_{0.05}MnO_2$.

This phenomenon is known as charge screening and can lead to a decrease in specific capacitance.

The effect of different scan rates on CV profile of $Ag_{0.05}MnO_2$ NWs was also studied. Fig. 10(b) displays the CV curves of

$Ag_{0.05}MnO_2$ at different scan rates. With an increase in scan rate, loop area also increases resulting in an increase in specific capacitance. The enlarged loop area is attributed to the fact that increasing the sweep rate enables more current to flow through the electrode material.

To conclude whether the prominent charge storage process is a pseudocapacitive or electric double layer, the power law relation was used.

$$i = a\nu^b \quad (4)$$

By taking $\log \nu$ on the x-axis, and $\log i$ on the y-axis, and plotting its linear fit gives the value of the slope and intercept. The slope value ranges between 0.5 and 1. For a perfect pseudocapacitor, the slope is 0.5, and for an ideal EDLC it is 1. The linear fit plot of $\log \nu$ *vs.* $\log i$ is given in Fig. 10(c). The inset of Fig. 10(c) illustrates the slope value, which is 0.62. It shows that the prominent charge storage process is pseudocapacitive.

Impact of scan rate on the charge storage mechanism was also investigated by Dunn's method given in eqn (5) and (6).[73]

$$i(\nu) = K_1\nu + K_2\nu^{1/2} \quad (5)$$

$$i(\nu)/\nu^{1/2} = K_1\nu^{1/2} + K_2 \quad (6)$$

The results obtained by using the above relations are shown in Fig. 10(d). By increasing the scan rate, the capacitive contribution towards total capacitance increased from 27% to 45%. This increase is due to the reduced time accessible for electrolyte ions to permeate the electrode material at a high scan rate. However, the diffusion-controlled charge storage process is prominent and its contribution towards total capacitance at all the scan rates is dominant suggesting the pseudocapacitive nature of the electro-active material.

The capacitance value for pristine and Ag doped MnO_2 NWs was calculated from the galvanostatic charge discharge (GCD) profile, which is obtained in the same range as that of CV. Comparative GCD measurements of all the samples performed at 1 A g^{-1} current density are shown in Fig. 11(a). The highest discharging time of 616 s was shown by $Ag_{0.05}MnO_2$ among all the samples. This suggests that the optimum concentration of Ag into MnO_2 is 0.05. The discharging time showed by other samples is 342 s, 400 s, and 480 s for MnO_2 NWs, $Ag_{0.15}MnO_2$, and $Ag_{0.10}MnO_2$ NWs respectively. The specific capacitance was

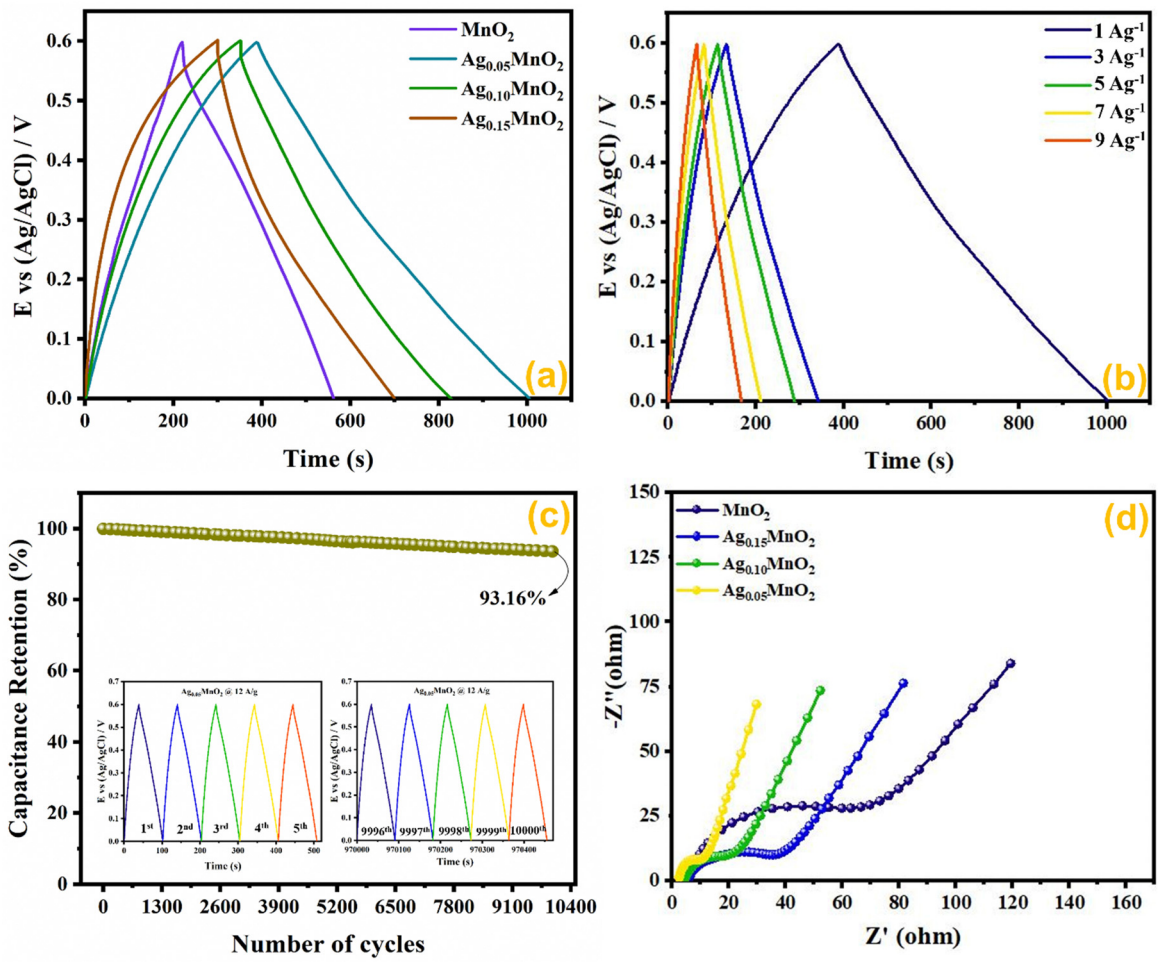

Fig. 11 (a) GCD curves of Ag_xMnO_2, (b) impact of varying current densities on GCD profile of $Ag_{0.05}MnO_2$, (c) capacitance retention after 10 000 GCD cycles (inset: first and last 5 cycles during cyclic test of $Ag_{0.05}MnO_2$), and (d) EIS profile of Ag_xMnO_2.

determined from GCD profiles using eqn (7).

$$C_{sp} = \frac{I \times \Delta t}{m \times \Delta V} \quad (7)$$

$Ag_{0.05}MnO_2$ exhibited the highest specific capacitance of 1027 F g^{-1}@1 A g^{-1} current density. This improvement is ascribed to the introduction of new gap states between the conduction and the valence band induced by the hybridization between Ag 4d with O 2p. Large size of Ag^+ ions and high energy of Ag 4d orbitals result in a strong repulsion between Ag 4d and O 2p which pushes energy levels upward causing fermi level to shift closer to conduction band. Moreover, oxygen and interstitial defects produced by silver doping also induced new occupied states between the conduction and the valence band resulting in an upward movement of the Fermi level. Thus, silver doping induced n-type characteristics in MnO_2.[74] The order of specific capacitance for different MnO_2 samples follows the order: $Ag_{0.05}MnO_2$ > $Ag_{0.10}MnO_2$ > $Ag_{0.15}MnO_2$ > MnO_2. The specific capacitance of all the electro-active materials is given in Table 2. It is observed that as the silver concentration exceeds 0.05 molar, the specific capacitance decreases by increasing the dopant concentration. Doping introduces impurities into the material, which can create defects or dislocations in the crystal lattice. At low doping concentrations, these defects can enhance the electrochemical surface area, thereby increasing the specific capacitance. However, at high doping concentrations, the excessive defects can lead to increased charge scattering, decreased electrolyte penetration, and increased resistance, resulting in a decrease in specific capacitance. It is inferred from the GCD profile of all the samples that MnO_2 showed an IR drop in the beginning of the discharge curve, which almost disappeared for $Ag_{0.05}MnO_2$. However, this IR drop again increased for $Ag_{0.10}MnO_2$ and $Ag_{0.15}MnO_2$. This decrease in IR drop for $Ag_{0.05}MnO_2$ is ascribed to the decreased resistivity of the electrode material.[75,76] GCD curve of MnO_2 is the characteristic curve of α-MnO_2.[77] With Ag doping, the GCD curve has become steeper and consistent with the already reported GCD curves of α-MnO_2.[67,78] It is due to the improved reaction kinetics, increased conductivity and shorter diffusion path of ions.

The impact of current densities on $Ag_{0.05}MnO_2$ NWs was also investigated. It can be assessed from Fig. 11(b) that by increasing the current density specific capacitance was decreased. However, the shape of the charging/discharging curve remains virtually the same.

Table 2 Specific capacitance and resistance values for all the prepared samples

S. no.	Sample	Specific capacitance (F g^{-1})	Charge transfer resistance (R_{ct}/Ω)	Solution resistance (R_s/Ω)
1	MnO_2	570	70	5.97
2	$Ag_{0.05}MnO_2$	1027	10	2.35
3	$Ag_{0.10}MnO_2$	800	20	4.16
4	$Ag_{0.15}MnO_2$	667	40	5.58

Table 3 Impact of varying current density on the specific capacitance of $Ag_{0.05}MnO_2$ NWs

S. no.	Current density (A g^{-1})	Specific capacitance (F g^{-1})	Retention (%)
1	1	1027	100
2	3	998	97
3	5	950	93
4	7	920	89
5	9	890	86

It is inferred from Table 3 that an increase in current density resulted in a decrease in specific capacitance. It might be ascribed to slow redox reaction at elevated current densities. Moreover, at lower current densities electrolyte ions not only adsorb on the surface but also penetrate the bulk. Consequently, more active sites are involved giving rise to an improved capacitance. Specific capacitance decreases when the current density is high because electrolyte ions are confined to the surface and do not have enough time to permeate the bulk. We also studied the cyclic stability of $Ag_{0.05}MnO_2$ NWs by applying 10,000 GCD cycles@12 A g^{-1}. The cyclic stability test findings are given in Fig. 11(c). The $Ag_{0.05}MnO_2$ electrode retained 93.16% of its initial capacitance. Inset of Fig. 11(c) shows the first five and last five GCD cycles. The excellent cyclic stability proved that doping a noble metal into the MnO_2 matrix is a good way to boost electrochemical performance of MnO_2. Table 4 compares the electrochemical performance of the current electrode material with the recent literature.

EIS measurements provide information about the mass transfer resistance, internal resistance, and resistance present at the electrode–electrolyte interface. EIS measurements for Ag_xMnO_2 NWs were performed in the frequency ranging between 0.1 Hz and 100 kHz, and are illustrated in Fig. 11(d). A typical EIS spectrum entails an x-intercept followed by a semicircle and a linear line in a low frequency region representing electrode–electrolyte interfacial resistance, charge transfer resistance (R_{ct}), and mass transfer resistance respectively. $Ag_{0.05}MnO_2$ NWs showed the smallest diameter indicating the smallest charge transfer resistance. It can be credited to Ag doping, which provided a new pathway for rapid electron transfer. The introduction of silver provide ions in the tunnels of MnO_2 leading to an improvement in conductivity. The resistance values are depicted in Table 2. It is observed that when doping concentration exceeds x = 0.05 the R_{ct} increases. It is ascribed to the fact that heavy doping causes pinning of the Fermi level near the surface of the electro-active material, resulting in energy barrier change across the electrode–electrolyte interface, thus increasing resistance in charge transfer.[88,89] Additionally, high doping leads to more scattering centers which also resists the charge transfer at the electrode–electrolyte interface.[90]

3.10. Mott–Schottky (M–S) analysis

In order to assess the charge carrier density and flat band potential M–S studies were performed. M–S profiles of $Ag_{0.05}MnO_2$ and $Ag_{0.15}MnO_2$ are illustrated in Fig. 12. The slope

Table 4 Comparison of the current electrode material with previously reported studies

Electroactive material	Specific capacitance (F g^{-1})	Retention (%)	Cyclic activity (%)/cycles	Ref.
F–MnO_2	148/0.5 A g^{-1}	100@10 A g^{-1}	82.80/10 000	79
Fe–MnO_2	196/1 A g^{-1}	70@30 A g^{-1}	83.3/20 000	80
K–MnO_2	283.7/1 A g^{-1}	66.9@20 A g^{-1}	90.7/10 000	81
Na–MnO_2	324.7/0.5 A g^{-1}	56.1@50 A g^{-1}	91/10 000	82
MnO_2/MXene	457/1 A g^{-1}	—	102.5/1000	83
Eu–MnO_2	362.1/1 A g^{-1}	63@10 A g^{-1}	100/10 000	84
Zn–MnO_2	392/1 A g^{-1}	70.4@20 A g^{-1}	94.3/10 000	85
Ag–MnO_2	520.8/0.5 A g^{-1}	—	90.6/2000	86
Ag–MnO_2/GO	868/2 A g^{-1}	49.1@5 A g^{-1}	94.5/5000	87
$Ag_{0.05}MnO_2$	1027/1 A g^{-1}	86%@9 A g^{-1}	93.16%/10 000	This work

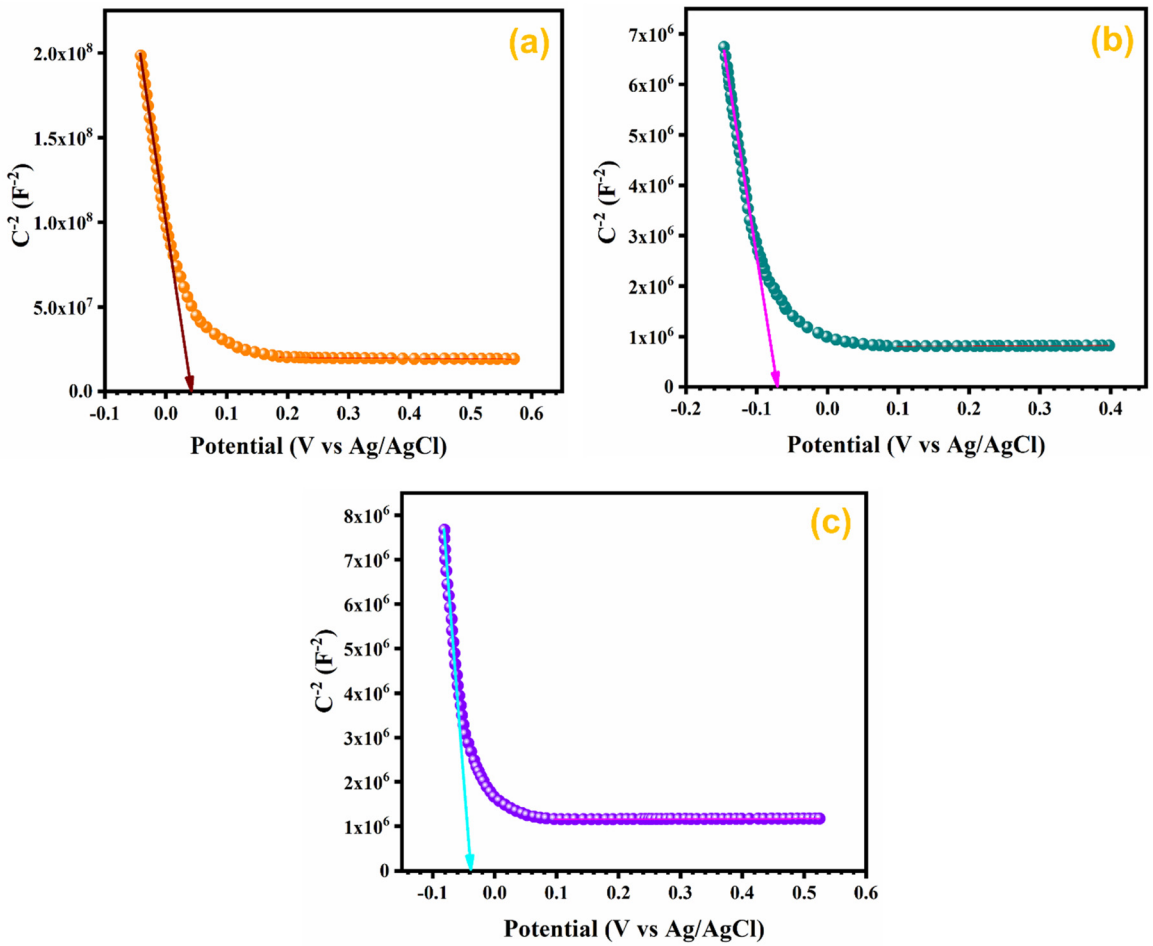

Fig. 12 M–S profile of (a) MnO_2, (b) $Ag_{0.05}MnO_2$, and (c) $Ag_{0.15}MnO_2$.

of the M–S plot for MnO_2 is negative, which suggests the p-type nature of the material,[91] while the slope of $Ag_{0.05}MnO_2$ and $Ag_{0.15}MnO_2$ is positive, indicating that doping has induced n-type character in MnO_2.[92–94] This transformation from p-type to n-type is associated with the production of oxygen vacancies. Production of oxygen vacancies is the result of charge balance which is caused by doping silver in MnO_2 due to variation in oxidation state of Ag^+ and Mn^{4+}. As a result of oxygen vacancy generation, electrons (charge carriers) will be left behind. Thus, the concentration of electrons will increase.[95] The flat band potentials of MnO_2, $Ag_{0.05}MnO_2$, and $Ag_{0.15}MnO_2$ are 0.042 V, −0.07 V, and −0.04 V respectively. The charge carrier densities of MnO_2, $Ag_{0.05}MnO_2$ and $Ag_{0.15}MnO_2$ are given in Table 1. Charge carrier density calculated from the M–S plot was found to increase with an increase in the Ag content. Bappi *et al.* have reported that doping induces scattering centers.[71] Heavy doping induced more scattering centers (increased charge carrier density) which increased the energy barrier at the electrode–electrolyte interface giving rise to an increase in R_{ct} and reduced mobility of charge carriers which is also confirmed by EIS and *I–V* measurements respectively.

4. Conclusions

In summary, a facile and low-temperature hydrothermal process has been used to synthesize Ag_xMnO_2 NWs. The effect of Ag doping on the structure and morphology has been validated by physico-chemical techniques. The influence of the dopant amount on electrochemical performance was also studied. XRD analysis showed a shift in the diffraction angle towards a lower 2θ value. FESEM analysis displayed cracks on the NWs' surface by Ag doping in MnO_2 NWs. BET studies revealed an increase in the surface area. Electrochemical investigations were carried out using porous 3D nickel foam as a current collector. Cyclic voltammetry investigations showed typical redox peaks in positive and negative current regions suggesting a prominent pseudocapacitive charge storage process. $Ag_{0.05}MnO_2$ NWs had a significantly higher specific capacitance of 1027 F g^{-1} in comparison to bare MnO_2@1 A g^{-1}. Furthermore, $Ag_{0.05}MnO_2$ showed lower resistance compared to other samples and excellent capacitance maintenance (93.16% at 12 A g^{-1} after 10 000 cycles). $Ag_{0.05}MnO_2$'s superior electrochemical performance is ascribed to increased conductivity, Ag intercalation into (2×2) tunnels and a shorter diffusion path length for electrolyte ions.

Author contributions

Muhammad Usman Khalid: investigation, data curation, and writing – review & editing; Sonia Zulfiqar: formal analysis, validation, and writing – review & editing; Imran Shakir: formal analysis; M. Nazirduddin Khan: resources; Muhammad Farooq Warsi: supervision and project administration; Eric W. Cochran: resources and project administration.

Conflicts of interest

There are no conflicts of interest to declare.

Acknowledgements

The researchers wish to extend their sincere gratitude to the Deanship of Scientific Research at the Islamic University of Madinah for the support provided to the Post-Publishing Program. Prof. Dr Sonia Zulfiqar is highly thankful for the support provided by the Statutory City of Ostrava, Czechia through Research Grant "Global Experts" and to the American University in Cairo, Egypt for using STRC facilities. Profs Cochran and Zulfiqar are grateful for the TEM imaging provided by Dr Tracey Stewart of the Roy J. Carver High Resolution Microscopy Facility and for the XPS measurements provided by Dr Dapeng Jing of the Materials Analysis and Research Laboratory of the Iowa State University Office of Biotechnology. E. W. C. and S. Z. are also thankful to the National Science Foundation for financial support through research grants NSF-2113695, NSF-2218070 and NSF-2242763.

References

1 A. K. Worku, D. W. Ayele, N. G. Habtu and M. D. Ambaw, *Heliyon*, 2022, **8**, e10960.
2 H. R. Barai, A. N. Banerjee and S. W. Joo, *J. Ind. Eng. Chem.*, 2017, **56**, 212–224.
3 Q. Liu, S. Ji, J. Yang, H. Wang, B. G. Pollet and R. J. M. Wang, *Materials*, 2017, **10**, 988.
4 J. Li, S. Yi, R. Rajagopalan, Z. Zhang, Y. Tang and H. Wang, *Green Energy Environ.*, 2023, **8**, 308–317.
5 V. J. Mane, S. B. Kale, S. B. Ubale, V. C. Lokhande and C. D. Lokhande, *Mater. Today Chem.*, 2021, **20**, 100473.
6 P. Simon, Y. Gogotsi and B. J. S. Dunn, *Science*, 2014, **343**, 1210–1211.
7 Y. Xiang, S. Lu and S. P. Jiang, *Chem. Soc. Rev.*, 2012, **41**, 7291–7321.
8 C. Liu, F. Li, L. P. Ma and H. M. Cheng, *Adv. Mater.*, 2010, **22**, E28–E62.
9 D. P. Dubal, N. R. Chodankar, D.-H. Kim and P. Gomez-Romero, *Chem. Soc. Rev.*, 2018, **47**, 2065–2129.
10 T. Xiong, T. L. Tan, L. Lu, W. S. V. Lee and J. J. A. E. M. Xue, *Adv. Energy Mater.*, 2018, **8**, 1702630.
11 P. Simon and Y. Gogotsi, *Nat. Mater.*, 2008, **7**, 845–854.
12 N. B. Velhal, N. C. Maile, C. Paeng, H. Lee, T. Kim, J. Kim and C. Yim, *J. Energy Storage*, 2024, **90**, 111764.
13 K. Kalaiselvi, M. Mubarak Ali, S. Prabhu, P. Muthu Mareeswaran and R. Ramesh, *Inorg. Chem. Commun.*, 2024, **162**, 112145.
14 J.-Z. Jiang, Y.-J. Gu, W. Wen, Z.-Z. Ye and J.-M. Wu, *J. Energy Storage*, 2024, **84**, 110957.
15 H. Li, H. Yang, H. Sun, Y. Huang, P. An, Y. Yunhua and H. Zhao, *Electrochim. Acta*, 2024, **473**, 143514.
16 H. A. Hamouda, S. Cui, X. Dai, X. Xie, H. Peng, G. Ma and Z. Lei, *J. Energy Storage*, 2022, **47**, 103616.
17 T. P. Manh, N. Nguyen Van, V. B. T. Phung, L. Ngo Thi, Q. Ngo Quy, S. Le The, P. Doan Tien, D. Tran Quang, T. Nguyen Van and N. To Van, *Ceram. Int.*, 2024, **50**, 22757–22770.
18 M. Imran, A. M. Afzal, M. W. Iqbal, H. H. Hegazy, M. Z. Iqbal, S. Mumtaz and R. Qureshi, *Mater. Sci. Semicond. Process.*, 2023, **158**, 107366.
19 I. Melkiyur, Y. Rathinam, P. S. Kumar, A. Sankaiya, S. Pitchaiya, R. Ganesan and D. Velauthapillai, *Renewable Sustainable Energy Rev.*, 2023, **173**, 113106.
20 S. Munir, M. Aadil, M. F. Warsi, H. H. Somaily, N. U. Ain and M. Shahid, *Ceram. Int.*, 2022, **48**, 33306–33314.
21 W. Guo, X. Lian, Y. Tian, T. Yang and S. Wang, *J. Energy Storage*, 2021, **38**, 102586.
22 S. Sun, G. Jiang, Y. Liu, B. Yu and U. Evariste, *J. Energy Storage*, 2018, **18**, 256–258.
23 T. P. Mofokeng, S. Shabalala, A. B. Haruna, P. V. Mwonga, Z. N. Tetana and K. I. Ozoemena, *J. Electroanal. Chem.*, 2023, **948**, 117809.
24 K. Li, C. Chen, H. Zhang, X. Hu, T. Sun and J. Jia, *Appl. Surf. Sci.*, 2019, **496**, 143662.
25 M. U. Khalid, K. M. Katubi, S. Zulfiqar, Z. A. Alrowaili, M. Aadil, M. S. Al-Buriahi, M. Shahid and M. F. Warsi, *Fuel*, 2023, **343**, 127946.

26 D. Gangwar and C. Rath, *Appl. Surf. Sci.*, 2021, **557**, 149693.
27 C. Ling, R. Zhang, T. S. Arthur and F. Mizuno, *Chem. Mater.*, 2015, **27**, 5799–5807.
28 E. Hastuti, A. Subhan, P. Amonpattaratkit, M. Zainuri and S. Suasmoro, *RSC Adv.*, 2021, **11**, 7808–7823.
29 K. Chen, W. Pan and D. Xue, *J. Phys. Chem. C*, 2016, **120**, 20077–20081.
30 X. Duan, J. Yang, H. Gao, J. Ma, L. Jiao and W. Zheng, *CrystEngComm*, 2012, **14**, 4196–4204.
31 J. Liu, J. Bao, X. Zhang, Y. Gao, Y. Zhang, L. Liu and Z. Cao, *RSC Adv.*, 2022, **12**, 35556–35578.
32 M. Thomas, W. Sun and J. Cui, *J. Phys. Chem. C*, 2012, **116**, 6383–6391.
33 S. G. Hassan and E. J. Mohammad, *Mater. Today: Proc.*, 2021, **42**, 2749–2751.
34 A. U. Rahman, N. Zarshad, J. Wu, F. Faiz, F. Raziq, A. Ali, G. Li and H. Ni, *Mater. Sci. Eng., B*, 2021, **269**, 115150.
35 G. Zhang, L. Zheng, M. Zhang, S. Guo, Z.-H. Liu, Z. Yang and Z. Wang, *Energy Fuels*, 2012, **26**, 618–623.
36 Y. Dai, S. Tang, S. Vongehr and X. Meng, *ACS Sustainable Chem. Eng.*, 2014, **2**, 692–698.
37 E. Umeshbabu, M. Satyanarayana, G. Karkera, A. Pullamsetty and P. J. M. A. Justin, *Mater. Adv.*, 2022, **3**, 1642–1651.
38 X. Wang and Y. J. C. A. E. J. Li, *Chem. – Eur. J.*, 2003, **9**, 300–306.
39 S. Mourdikoudis, R. M. Pallares and N. T. K. Thanh, *Nanoscale*, 2018, **10**, 12871–12934.
40 A. Alalawi, U. E. Romman, K. M. Katubi, S. T. Shafa, M. Usman Khalid, Z. A. Alrowaili, M. S. Al-Buriahi, M. I. Din and I. Shakir, *Curr. Appl. Phys.*, 2024, **60**, 32–42.
41 B. Rajesh Kumar and B. Hymavathi, *Adv. Nat. Sci.: Nanosci. Nanotechnol.*, 2018, **9**, 035018.
42 B. Bashir, M. U. Khalid, M. Aadil, S. Zulfiqar, M. F. Warsi, P. O. Agboola and I. J. C. I. Shakir, *Ceram. Int.*, 2021, **47**, 3603–3613.
43 R. Karmakar, S. K. Neogi, A. Banerjee and S. Bandyopadhyay, *Appl. Surf. Sci.*, 2012, **263**, 671–677.
44 Y. Gu, Y. Min, L. Li, Y. Lian, H. Sun, D. Wang, M. H. Rummeli, J. Guo, J. Zhong and L. Xu, *Chem. Mater.*, 2021, **33**, 4135–4145.
45 H. Usui, S. Suzuki, Y. Domi and H. Sakaguchi, *ACS Sustainable Chem. Eng.*, 2020, **8**, 9165–9173.
46 M. U. Khalid, M. F. Warsi, M. I. Sarwar, P. O. Agboola, I. Shakir and S. Zulfiqar, *Ceram. Int.*, 2020, **46**, 14287–14298.
47 M. F. Warsi, B. Bashir, S. Zulfiqar, M. Aadil, M. U. Khalid, P. O. Agboola, I. Shakir, M. A. Yousuf and M. J. C. I. Shahid, *Ceram. Int.*, 2021, **47**, 5044–5053.
48 D. Prieur, W. Bonani, K. Popa, O. Walter, K. W. Kriegsman, M. H. Engelhard, X. Guo, R. Eloirdi, T. Gouder, A. Beck, T. Vitova, A. C. Scheinost, K. Kvashnina and P. Martin, *Inorg. Chem.*, 2020, **59**, 5760–5767.
49 M. Siddiq, A. G. Taki, M. Aadil, S. Mubarik, E. W. Cochran, S. Zulfiqar, A. A. A. Mohammed and S. Ijaz, *Ceram. Int.*, 2023, **49**, 36590–36599.
50 M. Rashid, W. Hassan, M. Aadil, H. H. Somaily, N. M. Mahdi, R. Lataef, A. G. Taki, K. Srithilat, D. F. Baamer, S. M. Albukhari, M. A. Salam and A. Llyas, *Opt. Mater.*, 2023, **135**, 113192.
51 H. S. N. Jayawardena, S. H. Liyanage, K. Rathnayake, U. Patel and M. Yan, *Anal. Chem.*, 2021, **93**, 1889–1911.
52 M. V. Ananth, S. Pethkar and K. Dakshinamurthi, *J. Power Sources*, 1998, **75**, 278–282.
53 D. P. Dubal, W. B. Kim and C. D. Lokhande, *J. Phys. Chem. Solids*, 2012, **73**, 18–24.
54 Y. Khan, H. Sadia, S. Z. Ali Shah, M. N. Khan, A. A. Shah, N. Ullah, M. F. Ullah, H. Bibi, O. T. Bafakeeh and N. B. J. C. Khedher, *Catalysts*, 2022, **12**, 1386.
55 S. Yousaf, S. Zulfiqar, M. Shahid, A. Jamil, I. Shakir, P. O. Agboola and M. F. Warsi, *Ceram. Int.*, 2020, **46**, 14304–14310.
56 M. F. Warsi, M. Bilal, S. Zulfiqar, M. U. Khalid, P. O. Agboola and I. Shakir, *Mater. Res. Express*, 2020, **7**, 105015.
57 W. Zhang, *Nanomaterial*, 2014, 19–43.
58 W. Zhou and H. Greer, *Eur. J. Inorg. Chem.*, 2016, 941–950.
59 S. M. Jadhav, R. S. Kalubarme, N. Suzuki, C. Terashima, J. Mun, B. B. Kale, S. W. Gosavi and A. Fujishima, *ACS Omega*, 2021, **6**, 5717–5729.
60 S. Liu, L. Kang, J. Zhang, S. C. Jun and Y. J. N. A. M. Yamauchi, *NPG Asia Mater.*, 2023, **15**, 9.
61 L.-T. Tseng, Y. Lu, H. M. Fan, Y. Wang, X. Luo, T. Liu, P. Munroe, S. Li and J. Yi, *Sci. Rep.*, 2015, **5**, 9094.
62 A. d'Alfonso, B. Freitag, D. Klenov and L. J. P. R. B. Allen, *Phys. Rev. B: Condens. Matter Mater. Phys.*, 2010, **81**, 100101.
63 F. A. Stevie and C. Donley, *J. Vac. Sci. Technol., A*, 2020, **38**, 063204.
64 J. Kim, Y. H. Min, N. Lee, E. Cho, K. Y. Kim, G. Jeong, S. K. Moon, M. Joo, D. B. Kim and J. Kim, *ACS Omega*, 2017, **2**, 7424–7432.
65 B. Wei, L. Wang, Q. Miao, Y. Yuan, P. Dong, R. Vajtai and W. J. C. Fei, *Carbon*, 2015, **85**, 249–260.
66 M. Li, W. Lei, Y. Yu, W. Yang, J. Li, D. Chen, S. Xu, M. Feng and H. J. N. Li, *Nanoscale*, 2018, **10**, 15926–15931.
67 J. Cremonezzi, D. Tiba and S. Domingues, *SN Appl. Sci.*, 2020, **2**, 1689.
68 K. Rajkumari, D. Das, G. Pathak and S. Rokhum, *New J. Chem.*, 2019, **43**, 2134–2140.
69 Y. Pei, X. Chen, D. Xiong, S. Liao and G. J. P. O. Wang, *PLoS One*, 2013, **8**, e81627.
70 W. Zhang, X. Li, S. Liu, J. Qiu, J. An, J. Yao, S. Zuo, B. Zhang, H. Xia and C. J. C. Li, *ChemSusChem*, 2022, **15**, e202102158.
71 M. B. Pramanik, M. A. Al Rakib, M. A. Siddik, S. Bhuiyan and T. Research, *Eur. J. Eng. Technol. Res.*, 2024, **9**, 10–15.
72 S. Thomas, R. Thomas, A. K. Zachariah and R. Kumar, *Thermal and rheological measurement techniques for nanomaterials characterization*, Elsevier, 2017.
73 T. Brezesinski, J. Wang, S. H. Tolbert and B. Dunn, *Nat. Mater.*, 2010, **9**, 146–151.
74 M. A. Thomas, W. W. Sun and J. B. Cui, *J. Phys. Chem. C*, 2012, **116**, 6383–6391.
75 S. Dalvand, Z. Khoushab, S. M. Mousavi-Khoshdel, H. Ghafuri, H. R. E. Zand and M. Omidvar, *Int. J. Hydrogen Energy*, 2023, **48**, 10098–10107.

76 S. Yousaf, M. Aadil, S. Zulfiqar, M. F. Warsi, P. O. Agboola, M. F. Aly Aboud and I. Shakir, *J. Mater. Res. Technol.*, 2020, **9**, 14158–14167.
77 E. A. Arkhipova, A. S. Ivanov, K. I. Maslakov, R. Y. Novotortsev, S. V. Savilov, H. Xia, A. V. Desyatov and S. M. J. I. Aldoshin, *Ionics*, 2022, **28**, 3501–3509.
78 M. Mahmood, A. Rasheed, I. Ayman, T. Rasheed, S. Munir, S. Ajmal, P. O. Agboola, M. F. Warsi and M. Shahid, *Energy Fuels*, 2021, **35**, 3469–3478.
79 A. Xia, J. Li, X. Zeng, J. Chen and G. Tan, *Ceram. Int.*, 2024, **50**, 13061–13069.
80 L. Zhang, X. Li, L. Li, X. Cheng, H. Wu and J. Zheng, *J. Energy Storage*, 2024, **85**, 111136.
81 X. Zhang, F. Zhang, D. Wei, Z. Cai, Y. Song and X. Wang, *J. Energy Storage*, 2023, **72**, 108468.
82 H. Bai, S. Liang, T. Wei, Q. Zhou, M. Shi, Z. Jiang, J. Feng, M. Zhang and Z. Fan, *J. Power Sources*, 2022, **523**, 231032.
83 H. Peçenek, S. Yetiman, F. K. Dokan, M. S. Onses, E. Yılmaz and E. Sahmetlioglu, *Ceram. Int.*, 2022, **48**, 7253–7260.
84 Y. Liang, D. Zhu, S. Chao, M. Hu, D. Li, W. Zhou, J. Xu, X. Duan and P. Liu, *J. Energy Storage*, 2023, **60**, 106673.
85 J. Wu, W. Raza, P. Wang, A. Hussain, Y. Ding, J. Yu, Y. Wu and J. Zhao, *Electrochim. Acta*, 2022, **418**, 140339.
86 Y. Feng, H. Qu, Y. Wang, L. Wang, Y. Wang, D. Yang, B. Ding, Y. Sun, J. Guo and S. J. M. Dai, *Materials*, 2024, **17**, 1312.
87 V. Mane, S. Kale, S. Ubale, V. Lokhande and C. J. M. T. C. Lokhande, *Mater. Today Chem.*, 2021, **20**, 100473.
88 S. Wu, X. Yang, H. Huang, Z. Shen, Y. Xue, H. Yang, L. Wang, F. Xu, X. Wang and W. Ge, *Jpn. J. Appl. Phys.*, 2022, **61**, 090901.
89 J. M. d O. Cremonezzi, D. Y. Tiba and S. H. J. S. A. S. Domingues, *SN Appl. Sci.*, 2020, **2**, 1–9.
90 M. B. Pramanik, M. A. Al Rakib, M. A. Siddik, S. Bhuiyan and T. Research, *Eur. J. Eng. Technol. Res.*, 2024, **9**, 10–15.
91 S. Yousaf, K. M. Katubi, S. Zulfiqar, M. F. Warsi, Z. A. Alrowaili, M. S. Al-Buriahi and I. Ahmad, *Int. J. Hydrogen Energy*, 2023, **48**, 27201–27214.
92 S. Yousaf, S. Zulfiqar, H. H. Somaily, M. F. Warsi, A. Rasheed, M. Shahid and I. Ahmad, *RSC Adv.*, 2022, **12**, 23454–23465.
93 J. Jia, W. Yang, P. Zhang and J. Zhang, *Appl. Catal., A*, 2017, **546**, 79–86.
94 J. Ma, C. Wang and H. He, *Appl. Catal., B*, 2017, **201**, 503–510.
95 W. Du, X. Zhang, L. Wu, Z. Wang, W. Liu, J. Liu and F. Wang, in *Metal Oxide Defects*, ed. V. Kumar, S. Som, V. Sharma and H. C. Swart, Elsevier, 2023, pp. 491–531, DOI: **10.1016/B978-0-323-85588-4.00021-0**.